IEEE Access
Multidisciplinary | Rapid Review | Open Access Journal

Received 10 March 2024, accepted 20 March 2024, date of publication 29 March 2024, date of current version 4 April 2024.

Digital Object Identifier 10.1109/ACCESS.2024.3382983

RESEARCH ARTICLE

Redundancy-Driven Multi-Task Adaptive Backstepping Tracking Control for Aerial Manipulators

KAI-YUAN LIU, (Member, IEEE), TE-KANG HUNG, CHI-HUNG LIN, AND YEN-CHEN LIU, (Senior Member, IEEE)
Department of Mechanical Engineering, National Cheng Kung University (NCKU), Tainan 70101, Taiwan

Corresponding author: Yen-Chen Liu (yliu@mail.ncku.edu.tw)

This work was supported by the National Science and Technology Council (NSTC), Taiwan, under Grant NSTC 112-2636-E-006-001 and Grant NSTC 112-2628-E-006-014-MY3.

ABSTRACT This paper presents a novel multi-tasking control scheme for an aerial manipulator consisting of an unmanned aerial vehicle (UAV) and a robotic arm as a high degree-of-freedom (DOF) system. The decoupled dynamic model is investigated under uncertainties to precisely control the motion of the UAV and the robotic arm. To reduce unnecessary motion of the end-effector, the null-space behavioral (NSB) strategy is utilized to perform subtasks. This feature provides a smoother trajectory for the transported object. The convergence is theoretically analyzed by utilizing Lyapunov stability. The proposed control scheme is validated with numerical simulations and experiments in several scenarios. To verify the efficacy of the proposed method, two types of subtasks, joint angle limitation (JAL) and obstacle avoidance (OA), are presented to demonstrate the effectiveness of multi-tasking. Finally, experimental results for collision avoidance are provided to verify that the system can be implemented in practice. With the device's inherent noise, the root-mean-square error remains at approximately 5 cm for the UAV frame ZD850.

INDEX TERMS Autonomous aerial vehicles, manipulator dynamics, aerial manipulator, unmanned aerial vehicle, adaptive control, null space, null-space-based behavioral control.

I. INTRODUCTION

UAVs have emerged as significant contributors to the field of robotics research, primarily attributed to their exceptional maneuverability and operational capabilities. They find extensive application across various domains, including remote monitoring of hostile environments, surveillance operations, and cooperative transportation [1], [2], [3], [4], [5], [6]. The versatility and adaptability of UAVs have enabled their widespread deployment and utilization in diverse scenarios, making them integral to the advancement of robotic technology. Many researchers have been attracted by its practical potential and have developed several control strategies [7], [8], [9], [10], [11] and learning-based methods [12], [13], [14]. Both techniques have their features. Generally, control theories provide a valid analysis of stability and intuitive design direction, while learning-based methods can achieve tracking without the exact system model. To extend UAV applications, more users would like to consider UAVs that operate with additional tools mounted to interact with the object and the environment [15].

The tools equipped on UAVs in recent research can be categorized into three types, namely gripper, cable, and robot arm. The gripper can be attached directly to the bottom of the UAV to grab the object [16], [17], but its working envelope is limited due to its low DOF. UAVs equipped with cables present a relatively straightforward system structure, simplifying the analysis process. However, these systems face challenges when it comes to agile object transportation. The presence of cables adds complexity to the system's dynamics and control, as the cables introduce additional constraints and considerations that must be accounted for. Achieving agile and precise object transportation becomes more challenging due to the inherent limitations imposed by the cables. Therefore, additional design and control strategies are required to ensure efficient and accurate object

The associate editor coordinating the review of this manuscript and approving it for publication was Zheng Chen.

manipulation in such UAV systems. That is, the object can only be dragged according to the direction of the cable [18], [19], [20]. On the other hand, the UAV, with a robotic arm called an aerial manipulator, is endowed with high dexterity for 3D motion and more DOF than the aforementioned tools. Due to its privilege, the aerial manipulator attracts the attention of researchers.

A. RELATED WORKS

To design the behavior with better users' understanding, various control schemes have been recently proposed to take advantage of the feature of an aerial manipulator. In [21], task-constrained motion planning for aerial manipulators is investigated. The authors in [22] and [23] proposed controllers based on Euler-Lagrangian dynamic models of the overall system. The problem of disturbance from the environment is addressed in [24] by applying a robust method with numerical simulations. An optimization-based controller for multi-tasking aerial manipulators is proposed in [25]. To reach the specific performance criteria and deal with the disturbance, the method called adaptive prescribed performance control for aerial manipulators is investigated in [26] and [27]. However, the aforementioned works are developed with the exact model of overall aerial manipulators. The dimension of the model grows as the number of joints increases. Therefore, the computational burden to obtain the control signals also becomes considerably heavy. This concern is more critical to the embedded system with limited computational ability.

On the other hand, an alternative solution to address the computational issue is to develop control strategies with decoupled models of aerial manipulators. A decoupled model for an aerial manipulator is presented in [28] to show the effectiveness of controlling the UAV and the robotic arm separately. In [29], the authors presented the simulation with their decoupled strategy of force consensus for aerial manipulators' cooperation. The robust controllers with a decoupled model consisting of an underactuated UAV and a fully-actuated arm is proposed in [30]. In the subsequent work by [31], the model is expanded to incorporate the Deep Deterministic Policy Gradient (DDPG) algorithm for designing the control scheme for the robotic arm, along with the adaptive robust method employed for the UAV. Note that the methods in [28] and [31] are considered without the modeling of the robotic arm. This implicitly implies that the mass of the robotic arm should be light enough compared to that of the UAV. However, this fact also limits the DOF of the robotic arm because it could be considerably heavy with more actuators. Also, it is difficult to efficiently control the action of the robotic arm without considering its dynamics in the controller. To make use of the flexibility of the aerial manipulator, it is necessary to investigate further the dynamic model, including both the UAV and the robotic arm.

Another potential of an aerial manipulator is high redundancy thanks to the combination of a UAV and a robotic arm. The use of redundancy in robotic systems has recently been developed, and one of the famous methods is NSB control [32]. In conventional robotic arm research, the NSB method is considered to design subtasks while keeping the main objective working simultaneously and making the system multifunctional [33]. Moreover, an NSB controller is also designed for a multi-task aerial manipulator system in [34]. The authors of [35] and [36] introduce the controllers designed for a group of aerial manipulators utilizing the NSB method. However, the researches above only consider the kinematic model to design the controller. When operating the aerial manipulator, it is important to address how it interacts with both the object and the environment.

TABLE 1. Comparison with related works.

Paper	Modeling	Control	Multi-task	Boundary of disturbance
This work	Dynamics	Decoupled	Yes	No need
[35], [36]	Kinematics	Coupled	Yes	-
[25]	Dynamics	Coupled	Yes	-
[26]	Dynamics	Coupled	No	Estimated
[27]	Dynamics	Coupled	No	Estimated
[29]	Dynamics	Decoupled	No	Known
[31]	Dynamics	Decoupled	No	No need

B. MAIN CONTRIBUTIONS

To address the aforementioned challenges, this study presents a novel adaptive backstepping controller integrated with the null-space behavioral (NSB) approach for the aerial manipulator. The primary aim of this research is to ensure precise tracking of the end-effector while the system performs multiple tasks simultaneously. The key idea is alleviating the influence of the UAV to degrade the end-effector's tracking, which is not emphasized in related works. This feature can reduce unnecessary motion of the transported object in practice. To achieve this, the motion characteristics of the UAV and robotic arm are treated as distinct entities, and the respective dynamical models are derived by means of decoupling techniques. Based on the decoupled dynamic model, the adaptive backstepping controllers for the UAV and the arm are designed to separately track their own desired trajectories and compensate for system uncertainty. To exploit the redundancy for multi-tasks, the desired trajectories are generated by the NSB approach. Specifically, the subtasks are projected to the null space of the robotic arm's desired trajectory to ensure the end-effector's tracking is achievable. Moreover, the theoretical analysis is given by the Lyapunov Theorem to guarantee the convergence. To demonstrate the effectiveness of the proposed control scheme, the numerical examples with the JAL and OA subtasks are provided separately. Both cases show that the main task, trajectory tracking of the end-effector, and the subtask can be achieved simultaneously. Finally, the experimental data with a hexarotor and a 3-DOF robotic arm is included. The result shows that the proposed method still reaches the tracking with acceptable error under the noise and uncertainties in practice.

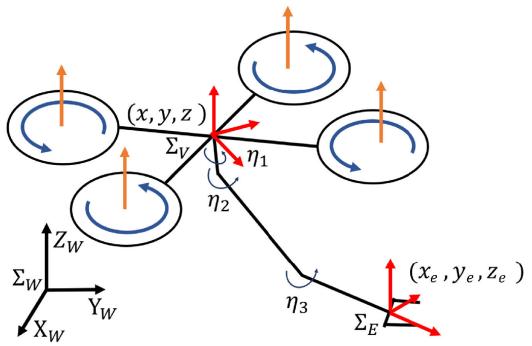

FIGURE 1. Coordinates of the aerial manipulator (a UAV with a 3-DOF robotic arm).

The contributions of this work are summarized below.

1) A decoupled dynamical model for aerial manipulator systems is proposed to deal with different DOFs in the robotic arm.
2) The adaptive controller ensures that the end-effector follows the desired trajectory under the uncertainties from the dynamics while the system's redundancy is assigned to perform subtasks and increase flexibility. Compared with the works [26], [27], our method doesn't require information about the boundary of the uncertainties or the disturbance.
3) A comprehensive discussion of different scenarios is included in the numerical examples and the results of the experiments. The efficacy of the proposed control scheme is validated in practice.

C. PAPER ORGANIZATION

The organization of the paper is as follows. Section II provides an overview of the UAV model, serving as a preliminary foundation for the subsequent discussions. Next, the novel decoupled model for aerial manipulators and the corresponding adaptive backstepping controller are proposed in Section III with theoretical analysis. To show the effectiveness of our method, the numerical examples in Section IV demonstrate the results with different subtasks. To confirm the effectiveness of the suggested method, we conducted an experiment using hardware consisting of a hexarotor and a robotic arm. Section V comprehensively presents the experimental study's details and results. In conclusion, Section VI summarizes the significant findings and highlights the contributions of this research.

II. PRELIMINARY

In this section, the dynamic model of the aerial manipulator is first introduced. To decouple the complex model, we start from the decoupled model for the UAV [31].

A. DYNAMICS OF AERIAL MANIPULATOR SYSTEM

The aerial manipulator system, including a UAV and a three-DOF robotic arm, is illustrated in Fig.1. The UAV's center of mass is where the body frame Σ_V is attached. The position $\mathbf{p} = [x, y, z]^T \in \mathbb{R}^3$ and orientation $\mathbf{\Theta} = [\phi, \theta, \psi]^T$ of the body frame Σ_V are defined with respect to the inertial frame Σ_W. Meanwhile, the robotic arm consisting of three revolute joints is mounted under the UAV, and its first joint rotates along the z-axis of Σ_V. The generalized coordinates of the robotic arm are defined as $\boldsymbol{\eta} \in \mathbb{R}^{n_r}$, and its end-effctor position is given as $\mathbf{p}_e = [x_e, y_e, z_e]^T \in \mathbb{R}^3$ with respect to Σ_W. Furthermore, the position $\mathbf{p}_i = [x_i, y_i, z_i]^T$ and the orientation $\mathbf{\Theta}_i = [\phi_i, \theta_i, \psi_i]^T$ of the center of mass for each link of the robotic arm are defined with respect to the body frame Σ_V. With the n_r-DOF robotic arm, the aerial manipulator system can perform flexible motion to meet task requirements.

To properly control the aerial manipulator system, it is necessary to derive the dynamics of the overall system. The generalized coordinates of the aerial manipulator system are given as $\mathbf{q} = [\mathbf{p}^T, \mathbf{\Theta}^T, \boldsymbol{\eta}^T]^T \in \mathbb{R}^n$ with $n = n_r + 6$, and the rotational matrix $\mathbf{R}_v \in SO(3)$ from Σ_V to Σ_W is defined by Euler z-x-y angles as

$$\mathbf{R}_v = \begin{bmatrix} c_\psi c_\theta - s_\phi s_\psi s_\theta & -c_\phi s_\psi & c_\psi s_\theta + c_\theta s_\phi s_\psi \\ c_\theta c_\psi + c_\psi s_\phi s_\theta & c_\phi c_\psi & s_\psi s_\theta - c_\psi c_\theta s_\phi \\ -c_\phi s_\theta & s_\phi & c_\phi c_\theta \end{bmatrix}, \quad (1)$$

where s_i, c_i stand for $sin(i), cos(i)$ respectively for $i = \{\phi, \theta, \psi\}$. Using the Euler-Lagrange equations, the dynamical model of the system with control input $\boldsymbol{\tau} \in \mathbb{R}^n$ is described as

$$\mathbf{M}(\mathbf{q})\ddot{\mathbf{q}} + \mathbf{C}(\mathbf{q}, \dot{\mathbf{q}})\dot{\mathbf{q}} + \mathbf{G}(\mathbf{q}) = \boldsymbol{\tau}, \quad (2)$$

where $\mathbf{M}(\mathbf{q}) \in \mathbb{R}^{n\times n}$ is the inertia matrix, $\mathbf{C}(\mathbf{q}, \dot{\mathbf{q}}) \in \mathbb{R}^{n\times n}$ is the Coriolis matrix, and $\mathbf{G}(\mathbf{q}) \in \mathbb{R}^n$ is the vector of gravitational force. According to the definitions above, the inertia matrix $\mathbf{M}(\mathbf{q})$ can be written as [37]

$$\mathbf{M}(\mathbf{q}) = \mathbf{M}_{t,b}^T m \mathbf{M}_{t,b} + \mathbf{M}_{r,b}^T \mathbf{R}_v I \mathbf{R}_v \mathbf{M}_{r,b} + \sum_{i=1}^{3} \mathbf{M}_{t,i}^T m_i \mathbf{M}_{t,i} + \mathbf{M}_{r,i}^T (\mathbf{R}_v \mathbf{R}_i) I_i (\mathbf{R}_i \mathbf{R}_v) \mathbf{M}_{r,i}. \quad (3)$$

where $\mathbf{M}_{t,b}, \mathbf{M}_{r,b}, \mathbf{M}_{t,i}, \mathbf{M}_{r,i} \in \mathbb{R}^{3\times n}$ are the matrices derived from the velocity of the components and the generalized coordinates, m, I is the mass and moment of inertia of the UAV respectively, m_i, I_i is those of the i^{th} link of the robotic arm, and R_i represents the rotational matrix from Σ_V to the center of the i^{th} link's mass. Moreover, the matrices $\mathbf{C}(\mathbf{q}, \dot{\mathbf{q}})$ and $\mathbf{G}(\mathbf{q})$ are derived by Christoffel symbols and the potential energy calculation, respectively.

Remark 1: The dynamic model can be applied to various types of aerial manipulators, regardless of the number of rotors on the UAV or the number of axes on the robotic arm. Additionally, there are no restrictions on the joint angles of the robotic arm.

B. DECOUPLED DYNAMIC MODEL OF UAV

The dynamics analysis discussed in Section II-A provides sufficient understanding and insight into controlling the motion of both the UAV and the robotic arm. The derived dynamics equations serve as a foundation for developing control strategies and designing effective controllers for the

coordinated movement of the aerial manipulator system. However, the computational complexity caused by $\mathbf{C}(\mathbf{q}, \dot{\mathbf{q}})$ makes it too intricate to run in real-time during flight. This problem is more severe for an embedded system with limited computational resources. Therefore, a decoupled UAV model derived from the Newton-Euler method is included to improve computational efficiency.

The decoupled dynamics from the Newton-Euler method are presented, assuming that the UAV operates with sufficient small roll and pitch to simplify the model. The dynamics of a UAV under the assumption of small angles is given as [38]

$$\begin{cases} m\ddot{\mathbf{p}} = \mathbf{R}F_t\boldsymbol{\mu}_3 - mg\boldsymbol{\mu}_3 \\ I\dot{\boldsymbol{\Omega}}_V = \boldsymbol{\tau}_s - \boldsymbol{\Omega}_V \times I\boldsymbol{\Omega}_V, \end{cases} \tag{4}$$

where F_t is the thrust force, $\boldsymbol{\Omega}_V$ is the angular velocity with respect to the body frame Σ_V, $\boldsymbol{\mu}_3 = [0, 0, 1]^T$. With the approximation $\boldsymbol{\Omega}_V = \dot{\boldsymbol{\Theta}} = [\dot{\phi}, \dot{\theta}, \dot{\psi}]^T$, the model of a UAV can be expressed as [31]

$$\begin{bmatrix} \ddot{x} \\ \ddot{y} \\ \ddot{z} \end{bmatrix} = \begin{bmatrix} c_\psi s_\theta + c_\theta s_\phi s_\psi \\ s_\theta s_\psi - s_\phi c_\theta c_\psi \\ c_\theta c_\phi \end{bmatrix} \frac{F_t}{m} - g\boldsymbol{\mu}_3, \tag{5}$$

$$\begin{bmatrix} \ddot{\phi} \\ \ddot{\theta} \\ \ddot{\psi} \end{bmatrix} = \begin{bmatrix} \Theta_\phi \dot{\theta}\dot{\psi} \\ \Theta_\theta \dot{\phi}\dot{\psi} \\ \Theta_\psi \dot{\phi}\dot{\theta} \end{bmatrix} + \begin{bmatrix} 1/I_x & 0 & 0 \\ 0 & 1/I_y & 0 \\ 0 & 0 & 1/I_z \end{bmatrix} \boldsymbol{\tau}_s, \tag{6}$$

where $\Theta_\phi = (I_y - I_z)/I_x$, $\Theta_\theta = (I_z - I_x)/I_y$, and $\Theta_\psi = (I_x - I_y)/I_z$. The moment applied to the system is denoted as $\boldsymbol{\tau}_s$.

Note that the dynamic model (5), (6) excludes the dynamics of the robotic arm and assumes that its weight is light enough to view as the disturbance for the UAV. As the robotic arm's DOF increases, the current model cannot be utilized to develop controllers for complex robotic arm motion. Thus, it is necessary to take further into account the model of the robotic arm to obtain better control performance for the high-DOF aerial manipulator system.

III. CONTROLLER DESIGN

In this section, the interaction between the UAV and the robotic arm is investigated with a modified dynamic model to release the weight limitation of the robotic arm in [31]. With the proposed model, the system can be separated into two parts, the UAV and the robotic arm, and then their controllers are separately designed.

A. DECOUPLED DYNAMIC MODEL OF AERIAL MANIPULATOR

To leverage the redundancy of the robotic arm, we propose a novel decoupled model for aerial manipulators that considers the arm's dynamics inspired by the aforementioned model (5) and (6). The DOF of the robotic arm is chosen as $n_r = 3$ for the redundancy. That is, we have $\boldsymbol{\eta} = [\eta_1, \eta_2, \eta_3]^T$. Let us denote the force F_d and moment $\boldsymbol{\tau}_d$ caused by the robotic arm on the UAV. Meanwhile, for the robotic arm, the control input $\boldsymbol{\tau}_{\eta s}$ and the influence $\boldsymbol{\tau}_{\eta d}$ due to the motion of the UAV are also defined. By taking the aforementioned terms into consideration with the model (5), (6), the dynamic model of the aerial manipulator can be rewritten as

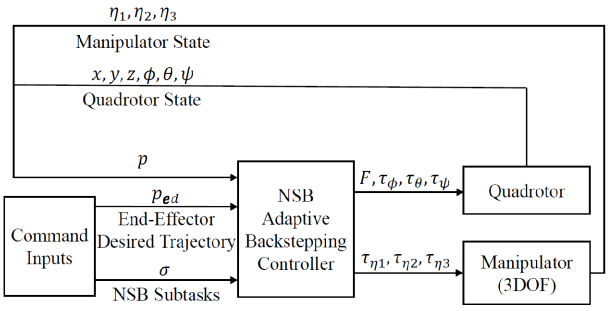

FIGURE 2. Block diagram of the aerial manipulator system.

$$\begin{bmatrix} \ddot{x} \\ \ddot{y} \\ \ddot{z} \end{bmatrix} = \begin{bmatrix} c_\psi s_\theta + c_\theta s_\phi s_\psi \\ s_\theta s_\psi - s_\phi c_\theta c_\psi \\ c_\theta c_\phi \end{bmatrix} \frac{F_s + F_d}{m} + \frac{\mathbf{F}_q}{m} + g\boldsymbol{\mu}_3, \tag{7}$$

$$\begin{bmatrix} \ddot{\phi} \\ \ddot{\theta} \\ \ddot{\psi} \end{bmatrix} = \begin{bmatrix} \Theta_\phi \dot{\theta}\dot{\psi} \\ \Theta_\theta \dot{\phi}\dot{\psi} \\ \Theta_\psi \dot{\phi}\dot{\theta} \end{bmatrix} + \mathbf{I}^{-1}(\boldsymbol{\tau}_s + \boldsymbol{\tau}_d + \boldsymbol{\tau}_q), \tag{8}$$

$$\begin{bmatrix} \ddot{\eta}_1 \\ \ddot{\eta}_2 \\ \ddot{\eta}_3 \end{bmatrix} = \begin{bmatrix} N_1 \\ N_2 \\ N_3 \end{bmatrix} + \mathbf{I}_\eta^{-1}\left(\boldsymbol{\tau}_{\eta s} + \boldsymbol{\tau}_{\eta d}\right), \tag{9}$$

where N_1, N_2, N_3 are the nonlinear item without $\ddot{\eta}$, $\mathbf{I} = diag\left\{I_x, I_y, I_z\right\}$, $\mathbf{I}_\eta$ are the inertia matrices of the UAV and robotic arm, respectively, and $\mathbf{F}_q, \boldsymbol{\tau}_q$ are the influence of uncertainties. So far, the behavior of the robotic arm affecting the overall system can be depicted with the proposed model.

B. ADAPTIVE BACKSTEPPING CONTROLLER WITH NSB APPROACH

1) REDUNDANCY-BASED DESIGN

Based on the dynamic model derived in Section III-A, the knowledge about the system is enough to build an advanced scheme for the challenge of various tasks. To better utilize the redundancy of the aerial manipulator system, the NSB strategy is applied to increase the flexibility of the UAV controller during operation. Namely, the system can not only let the end-effector track the desired trajectory but also perform subtasks like collision avoidance for the UAV simultaneously. The block diagram of the proposed design for the aerial manipulator system is illustrated in Fig. 2. Let us first define the desired trajectory of the aerial manipulator system $\mathbf{q}_d = [\mathbf{p}_d, \boldsymbol{\Theta}_d, \boldsymbol{\eta}_d]^T = [x_d, y_d, z_d, \phi_d, \theta_d, \psi_d, \eta_{1d}, \eta_{2d}, \eta_{3d}]^T \in \mathbb{R}^n$ and the tracking error $\mathbf{e} = \mathbf{q} - \mathbf{q}_d = [\mathbf{e}_p^T, \mathbf{e}_\Theta^T, \mathbf{e}_\eta^T]^T \in \mathbb{R}^n$, where $\mathbf{e}_p = \mathbf{p} - \mathbf{p}_d, \mathbf{e}_\Theta = \boldsymbol{\Theta} - \boldsymbol{\Theta}_d, \mathbf{e}_\eta = \boldsymbol{\eta} - \boldsymbol{\eta}_d \in \mathbb{R}^3$ are the error of the position and orientation of the UAV and the joint space of the robotic arm respectively. The update law of $\mathbf{q}_d$ using the NSB approach is designed as

$$\dot{\mathbf{q}}_d = \mathbf{J}_v^\dagger\left(\lambda \mathbf{e}_e + \dot{\mathbf{p}}_{ed}\right) + \left(\mathbf{I} - \mathbf{J}_v^\dagger \mathbf{J}_v\right)\boldsymbol{\sigma}, \tag{10}$$

where $\mathbf{e}_e = \mathbf{p}_e - \mathbf{p}_{ed}$ is the end-effector's position error, $\mathbf{J}_v \in \mathbb{R}^{3\times 9}$ is the velocity Jacobian matrix derived from the

relationship of $\dot{\mathbf{x}}_e$ and $\dot{\mathbf{p}}$, $\mathbf{J}_v^{\dagger} = \mathbf{J}_v^T \left(\mathbf{J}_v \mathbf{J}_v^T\right)^{-1}$ is the pseudo inverse matrix of $\mathbf{J}_v$, σ is the auxiliary function for the subtask which is explained later, and λ is a positive gain. The main purpose of (10) is to keep the subtasks such as collision avoidance of the UAV or joint constraints of the robotic arm in the null space of the control term for tracking the end-effector. That is, the system first tracks the desired position of the end-effector and then exploits the redundancy to perform subtasks.

This work presents two kinds of subtasks, joint angle limitation (JAL) and obstacle avoidance (OA) of the UAV. These subtasks are general and widely used in practice [39], so it is obvious for readers to understand their effectiveness in the proposed method. The auxiliary function $\boldsymbol{\sigma}$ is given as

$$\boldsymbol{\sigma} = -k_{sub}\mathbf{J}_{sub}, \tag{11}$$

where $\mathbf{J}_{sub} = \partial \mathbf{f}_{sub}/\partial \mathbf{q}$ is the Jacobian matrix of subtask function $\mathbf{f}_{sub} = \{\mathbf{f}_{lim}, \mathbf{f}_{ob}\}$ and k_{sub} is the gain for each subtask. The definitions of subtasks are as follows.

2) JOINT ANGLE LIMITATION (JAL)

This subtask can ensure the joint angles of the robotic arm to be operated in a pre-defined range [39]. The function f_{lim} is designed as

$$_{lim} = -\prod_{i=1}^{n}\left(\left(1 - \frac{\eta_i}{\eta_i^{max}}\right)\left(\frac{\eta_i}{\eta_i^{min}} - 1\right)\right), \tag{12}$$

where η_i^{max} is the maximum angle for the i^{th} joint, η_i^{min} is the minimum angle for the i^{th} joint, and η_i represents the i^{th} joint of the robotic arm.

3) OBSTACLE AVOIDANCE FOR UAV (OA)

This subtask can prevent the UAV from a collision when the UAV is close to the obstacle [39]. It is designed as

$$_{ob} = \left(min\left\{0, \frac{||\mathbf{p}_v - \mathbf{p}_{ob}||^2 - R^2}{||\mathbf{p}_v - \mathbf{p}_{ob}||^2 - r^2}\right\}\right)^2, \tag{13}$$

where $\mathbf{p}_v = [x, y, z]^T$, $\mathbf{p}_{ob} \in \mathbb{R}^3$, d is the distance between the UAV and the obstacle, R represents the distance to trigger this function, and r represents the shortest distance for safety. As d changes, the definition of J_{VOA} is

$$\mathbf{J}_{ob} = \begin{cases} 0 & if\ d \geq R \\ \partial \mathbf{f}_{ob}/\partial \mathbf{q} & if\ r < d < R \\ not\ defined & if\ d = r \\ 0 & if\ d < r. \end{cases} \tag{14}$$

Thus, this function can keep the UAV from the obstacle with a distance larger than r.

4) ADAPTIVE BACKSTEPPING TRACKING CONTROLLER

By considering the desired trajectories of the end-effector and the robotic arm as defined in Equation (10), an adaptive backstepping tracking controller is developed for the aerial manipulator system. Based on the decoupled dynamic model derived in (7)-(9), let us define the control inputs of the force $F = F_s + F_d$ and torque $\boldsymbol{\tau} = \boldsymbol{\tau}_s + \boldsymbol{\tau}_d$ of the UAV and the torque $\tau_\eta = \boldsymbol{\tau}_{\eta s} + \boldsymbol{\tau}_{\eta d}$ of the robotic arm, respectively. Inspired by the concept of nominal inputs, the force and torque inputs are represented as

$$F = \hat{m}\bar{F} - \mathbf{R}_\mu^{-1}\hat{\mathbf{F}}_q, \boldsymbol{\tau} = \hat{\mathbf{I}}\bar{\boldsymbol{\tau}} + \hat{\boldsymbol{\tau}}_q, \hat{\boldsymbol{\tau}}_\eta = \hat{\mathbf{I}}_\eta \bar{\boldsymbol{\tau}}_\eta \tag{15}$$

where $\bar{F}, \bar{\boldsymbol{\tau}}, \bar{\boldsymbol{\tau}}_\eta$ are the nominal inputs, $\hat{m} \in \mathbb{R}$ is the estimate of the equivalent mass of the UAV, $\hat{\boldsymbol{\tau}}_q = [\hat{\tau}_{xq}, \hat{\tau}_{yq}, 0]^T$, $\hat{\mathbf{I}} = diag\left\{\hat{I}_x, \hat{I}_y, \hat{I}_z\right\}, \hat{\mathbf{I}}_\eta \in \mathbb{R}^{3\times 3}$ are the estimate of the equivalent moment of inertia of the UAV and robotic arm, respectively. To track the desired trajectory without the exact knowledge of dynamic models, the tracking errors $\mathbf{e}_1, \mathbf{e}_2, \mathbf{e}_9, \mathbf{e}_{10} \in \mathbb{R}^3, e_3, e_4, e_5, e_6, e_7, e_8 \in \mathbb{R}$ are given as

$$\mathbf{e}_1 = \mathbf{e}_p,\ \mathbf{e}_2 = \dot{\mathbf{e}}_1 + \mathbf{k}_1\mathbf{e}_1,\ e_3 = \phi - \phi_d,\ e_4 = \dot{e}_3 + k_3 e_3, \tag{16}$$

$$e_5 = \theta - \theta_d, \quad e_6 = \dot{e}_5 + k_5 e_5, \quad e_7 = \psi - \psi_d, \tag{17}$$

$$e_8 = \dot{e}_7 + k_7 e_7, \quad \mathbf{e}_9 = \mathbf{e}_\eta, \quad \mathbf{e}_{10} = \dot{\mathbf{e}}_9 + \mathbf{k}_9\mathbf{e}_9, \tag{18}$$

where $\mathbf{k}_1, \mathbf{k}_9 \in \mathbb{R}^{3\times 3}$ are diagonal gain matrices, $k_3, k_5, k_7 \in \mathbb{R}$ are positive gains. Moreover, the nominal inputs are designed to be

$$\bar{F} = \mathbf{R}_\mu^{-1}\left(-\mathbf{e}_1 - \mathbf{k}_2\mathbf{e}_2 + g\boldsymbol{\mu}_3 + \ddot{p}_d - \mathbf{k}_1\dot{e}_1\right), \tag{19}$$

$$\bar{\boldsymbol{\tau}} = \begin{bmatrix} \bar{\tau}_x \\ \bar{\tau}_y \\ \bar{\tau}_z \end{bmatrix} = \begin{bmatrix} -e_3 - k_4 e_4 + \ddot{\phi}_d - k_3\dot{e}_3 - \hat{\Theta}_\phi \dot{\theta}\dot{\psi} \\ -e_5 - k_6 e_6 + \ddot{\theta}_d - k_5\dot{e}_5 - \hat{\Theta}_\theta \dot{\phi}\dot{\psi} \\ -e_7 - k_8 e_8 + \ddot{\psi}_d - k_7\dot{e}_7 - \hat{\Theta}_\psi \dot{\phi}\dot{\theta} \end{bmatrix} \tag{20}$$

$$\bar{\boldsymbol{\tau}}_\eta = -\mathbf{e}_9 - \mathbf{k}_{10}\mathbf{e}_{10} + \ddot{\boldsymbol{\eta}}_d - \mathbf{k}_9\dot{\mathbf{e}}_9 - \hat{\mathbf{N}}, \tag{21}$$

where $\mathbf{k}_2, \mathbf{k}_{10} \in \mathbb{R}^{3\times 3}$ are diagonal gain matrices, $k_4, k_6, k_8 \in \mathbb{R}$ are positive gains, $\mathbf{R}_\mu = \mathbf{R}_v\boldsymbol{\mu}_3$ is the last column of $\mathbf{R}_v$, $\hat{\Theta}_\beta, \hat{\mathbf{N}}$ are the estimates of $\Theta_\beta, \mathbf{N}$, respectively, for $\beta = \{\phi, \theta, \psi\}$, and $\hat{\mathbf{F}}_q, \hat{\tau}_{xq}, \hat{\tau}_{yq}$ are used to improve the UAV's tracking performance. Note that the position error $\mathbf{e}_p$ utilized in (16) is calculated from the position of end-effector $\mathbf{e}_e$ as $\mathbf{e}_q = J_v^{\dagger}\mathbf{e}_e$. To deal with the uncertainties of the dynamic model, the update laws of the estimation are designed as

$$\dot{\hat{m}} = -\gamma_m \mathbf{e}_2^T \bar{F}\mathbf{R}_\mu,\ \dot{\hat{I}}_x = -\gamma_{I_x} e_4 \bar{\tau}_x,\ \dot{\hat{I}}_y = -\gamma_{I_y} e_6 \bar{\tau}_y, \tag{22}$$

$$\dot{\hat{I}}_z = -\gamma_{I_z} e_8 \bar{\tau}_z,\ \dot{\hat{\mathbf{I}}}_\eta = -\gamma_{I_\eta}\mathbf{e}_{10}\bar{\boldsymbol{\tau}}_\eta^T,\ \dot{\hat{\mathbf{F}}}_q = \gamma_{F_q}\mathbf{e}_2, \tag{23}$$

$$\dot{\hat{\Theta}}_\phi = \gamma_\phi e_4 \dot{\theta}\dot{\psi},\ \dot{\hat{\Theta}}_\theta = \gamma_\theta e_4 \dot{\phi}\dot{\psi},\ \dot{\hat{\Theta}}_\psi = \gamma_\psi e_4 \dot{\phi}\dot{\theta}, \tag{24}$$

$$\dot{\hat{\tau}}_{xq} = -\gamma_{xq} e_4,\ \dot{\hat{\tau}}_{yq} = -\gamma_{yq} e_6,\ \dot{\hat{\mathbf{N}}} = \gamma_N \mathbf{e}_{10}, \tag{25}$$

where $\gamma_m, \gamma_{I_x}, \gamma_{I_y}, \gamma_{I_z}, \gamma_{I_\eta}, \gamma_{F_q}, \gamma_\phi, \gamma_\theta, \gamma_\psi, \gamma_{xq}, \gamma_{yq}, \gamma_N$ are positive parameters. Briefly, the adaptive laws are designed based on the concept of backstepping controllers to solve the tracking problems of the aerial manipulator.

C. STABILITY ANALYSIS

This subsection provides the theoretical analysis of the proposed adaptive backstepping controller for aerial manipulators. Before the discussion, the following assumption is first made.

Assumption 1: The rates of change of $\mathbf{F}_q, I_i, \Theta_j, \mathbf{I}_\eta$, *and* $\mathbf{N}$ *are sufficiently small for* $i \in \{x, y, z\}$ *and* $j \in \{\phi, \theta, \psi\}$.

Then, the theorem is proposed as follows.

Theorem 1: Consider an aerial manipulator system described by the decoupled dynamic model (7)-(9) with Assumption 1, the tracking errors of the system (16)-(18) converge to the origin asymptotically with the controllers (15),(19)-(21) and the adaptive laws (22)-(25).

Proof: Consider the positive-definite Lyapunov candidate $V = V_F + V_\tau + V_{\tau_\eta}$ such that

$$V_F = \frac{1}{2}\left(\sum_{i=1}^{2} \mathbf{e}_i^T \mathbf{e}_i + \frac{\tilde{m}^2}{\gamma_m m} + \frac{\tilde{\mathbf{F}}_q^T \tilde{\mathbf{F}}_q}{\gamma_{F_q} m}\right), \tag{26}$$

$$V_\tau = \frac{1}{2}\left(\sum_{i=3}^{8} \mathbf{e}_i^2 + \sum_{i\in\{\phi,\theta,\psi\}} \frac{\tilde{\Theta}_i^2}{\gamma_i} + \sum_{j\in\{x,y,z\}} \frac{\tilde{I}_j^2}{\gamma_{I_j} I_j}\right), \tag{27}$$

$$V_{\tau_\eta} = \frac{1}{2}\left(\sum_{i=9}^{10} \mathbf{e}_i^T \mathbf{e}_i + \frac{\tilde{\mathbf{N}}}{\gamma_N} \frac{\tilde{\mathbf{I}}_\eta^2}{\gamma_{I_\eta} \mathbf{I}_\eta}\right), \tag{28}$$

where $\tilde{m} = m - \hat{m}$, $\tilde{\Theta}_i = \Theta_i - \hat{\Theta}_i$, $\tilde{I}_j = I_j - \hat{I}_j$, $\tilde{\mathbf{I}}_\eta = \mathbf{I}_\eta - \hat{\mathbf{I}}_\eta$ for $i \in \{\phi, \theta, \psi\}$ and $j \in \{x, y, z\}$. Substituting $\dot{\mathbf{e}}_2 = \ddot{\mathbf{e}}_1 + \mathbf{k}_1 \dot{\mathbf{e}}_1$, the dynamics in (7), the controller in (19), and the adaptive law in (22), we have the time derivative of V_F as

$$\begin{aligned}
\dot{V}_F &= \mathbf{e}_1^T \dot{\mathbf{e}}_1 + \mathbf{e}_2^T \dot{\mathbf{e}}_2 - \frac{\tilde{m}\dot{\hat{m}}}{\gamma_m m} + \frac{\tilde{\mathbf{F}}_q^T \dot{\tilde{\mathbf{F}}}_q}{\gamma_{F_q} m} \\
&= \mathbf{e}_1^T \dot{\mathbf{e}}_1 + \mathbf{e}_2^T (\ddot{\mathbf{e}}_1 + \mathbf{k}_1 \dot{\mathbf{e}}_1) - \frac{\tilde{m}\dot{\hat{m}}}{\gamma_m m} + \frac{\tilde{\mathbf{F}}_q^T \dot{\tilde{\mathbf{F}}}_q}{\gamma_{F_q} m} \\
&= \mathbf{e}_1^T \dot{\mathbf{e}}_1 + \mathbf{e}_2^T \left(\frac{F}{m}\mathbf{R}_\mu + \frac{\mathbf{F}_q}{m} - g\boldsymbol{\mu}_3 - \ddot{\mathbf{p}}_d + \mathbf{k}_1 \dot{\mathbf{e}}_1\right) - \frac{\tilde{m}\dot{\hat{m}}}{\gamma_m m} \\
&\quad + \frac{\tilde{\mathbf{F}}_q^T \dot{\tilde{\mathbf{F}}}_q}{\gamma_{F_q} m} \\
&= \mathbf{e}_1^T (\mathbf{e}_2 - \mathbf{k}_1 \mathbf{e}_1) + \mathbf{e}_2^T (\bar{F}\mathbf{R}_\mu - g\boldsymbol{\mu}_3 - \ddot{\mathbf{p}}_d + \mathbf{k}_1 \dot{\mathbf{e}}_1) \\
&\quad - \frac{\tilde{m}}{\gamma_m m}\left(\dot{\hat{m}} + \gamma_m \mathbf{e}_2^T \bar{F}\mathbf{R}_\mu\right) + \mathbf{e}_2^T\left(-\frac{\hat{\mathbf{F}}_q}{m} + \frac{\mathbf{F}_q}{m}\right) + \frac{\tilde{\mathbf{F}}_q^T \dot{\hat{\mathbf{F}}}_q}{\gamma_{F_q} m} \\
&= -\mathbf{k}_1 \mathbf{e}_1^T \mathbf{e}_1 - \mathbf{k}_2 \mathbf{e}_2^T \mathbf{e}_2 \le 0.
\end{aligned} \tag{29}$$

According to Assumption 1, we have $\dot{\tilde{F}}_q = \dot{\hat{F}}_q - \dot{\mathbf{F}}_q \approx \dot{\hat{F}}_q$. Next, we define $V_{\tau,\phi} = e_3^2 + e_4^2 + \frac{\tilde{\Theta}_\phi^2}{\gamma_\phi} + \frac{\tilde{I}_x^2}{\gamma_{I_x} I_x}$ and have its time derivative as

$$\begin{aligned}
\dot{V}_{\tau,\phi} &= e_3 \dot{e}_3 + e_4 \dot{e}_4 + \frac{\tilde{\Theta}_\phi \dot{\tilde{\Theta}}_\phi}{\gamma_\phi} + \frac{\tilde{I}_x \dot{\tilde{I}}_x}{\gamma_{I_x} I_x} \\
&= e_3 (e_4 - k_3 e_3) + e_4 \left(\ddot{\phi} - \ddot{\phi}_d + k_3 e_3\right) - \frac{\tilde{\Theta}_\phi \dot{\tilde{\Theta}}_\phi}{\gamma_\phi} - \frac{\tilde{I}_x \dot{\tilde{I}}_x}{\gamma_{I_x} I_x} \\
&= e_3 (e_4 - k_3 e_3) + e_4 \left(\Theta_\phi \dot{\theta}\dot{\psi} + \frac{\hat{I}_x \bar{\tau}_x}{I_x} - \ddot{\phi}_d + k_3 \dot{e}_3\right) \\
&\quad - \frac{\tilde{\Theta}_\phi \dot{\tilde{\Theta}}_\phi}{\gamma_\phi} - \frac{\tilde{I}_x \dot{\tilde{I}}_x}{\gamma_{I_x} I_x}.
\end{aligned} \tag{30}$$

Note that

$$\frac{\hat{I}_x \bar{\tau}_x}{I_x} = \bar{\tau}_x - \frac{\tilde{I}_x \bar{\tau}_x}{I_x}. \tag{31}$$

Again under Assumption 1, we have $\dot{I}_i, \dot{\Theta}_j \approx 0$, which means $\dot{\tilde{I}}_i = -\dot{\hat{I}}_i$ and $\dot{\tilde{\Theta}}_j = -\dot{\hat{\Theta}}_j$ for $i \in \{x, y, z\}$ and $j \in \{\phi, \theta, \psi\}$. By substituting (31) and $\Theta_\phi = \tilde{\Theta}_\phi + \hat{\Theta}_\phi$, $\dot{V}_{\tau,\phi}$ is rearranged as

$$\begin{aligned}
\dot{V}_{\tau,\phi} &= e_3(e_4 - k_3 e_3) + e_4(\hat{\Theta}_\phi \dot{\theta}\dot{\psi} + \bar{\tau}_x - \ddot{\phi}_d + k_3 \dot{e}_3) \\
&\quad + \tilde{\Theta}_\phi (e_4 \dot{\theta}\dot{\psi} - \frac{\dot{\hat{\Theta}}_\phi}{\gamma_\phi}) - \frac{\tilde{I}_x(\dot{\hat{I}}_x + \gamma_{I_x} e_4 \bar{\tau}_x)}{\gamma_{I_x} I_x}.
\end{aligned} \tag{32}$$

By utilizing the adaptive laws (22)-(25), the last two terms in (32) equals to zero. Adopting the proposed controller 21, it is derived as

$$\begin{aligned}
\dot{V}_{\tau,\phi} &= e_3(e_4 - k_3 e_3) + e_4(\hat{\Theta}_\phi \dot{\theta}\dot{\psi} + \bar{\tau}_x - \ddot{\phi}_d + k_3 \dot{e}_3) \\
&= -k_3 e_3^2 - k_4 e_4^2 \le 0.
\end{aligned} \tag{33}$$

Following the similar procedure to define $V_{\tau,\theta}$ and $V_{\tau,\psi}$ for the remaining terms in V_τ, we obtain

$$\dot{V}_\tau = \dot{V}_{\tau,\phi} + \dot{V}_{\tau,\theta} + \dot{V}_{\tau,\psi} \le \sum_{i=3}^{8} k_i e_i^2 \le 0. \tag{34}$$

Furthermore, the time derivative of V_{τ_η} is given as

$$\dot{V}_{\tau_\eta} = e_9^T (\mathbf{e}_{10} - \mathbf{k}_9 e_9) + \mathbf{e}_{10}^T \left(\ddot{\eta} - \ddot{\boldsymbol{\eta}}_d + \mathbf{k}_9 \dot{e}_9\right) - \frac{\tilde{\mathbf{N}}\dot{\hat{\mathbf{N}}}}{\gamma_N} - \frac{\tilde{\mathbf{I}}_\eta \dot{\hat{\mathbf{I}}}_\eta}{\gamma_{I_\eta} \mathbf{I}_\eta}. \tag{35}$$

Note that

$$\frac{\hat{\mathbf{I}}_\eta \bar{\boldsymbol{\tau}}_\eta}{\mathbf{I}_\eta} = \bar{\boldsymbol{\tau}}_\eta - \frac{1}{\mathbf{I}_\eta} \tilde{\mathbf{I}}_\eta \bar{\boldsymbol{\tau}}_\eta. \tag{36}$$

Similarly, we obtain $\dot{\tilde{\mathbf{I}}}_\eta = -\dot{\hat{\mathbf{I}}}_\eta$ and $\dot{\tilde{\mathbf{N}}} = -\dot{\hat{\mathbf{N}}}$ under Assumption 1. With the dynamic model (9) and the definition (15), the equation (35) is rewritten as

$$\begin{aligned}
\dot{V}_{\tau_\eta} &= \mathbf{e}_9^T (\mathbf{e}_{10} - \mathbf{k}_9 \mathbf{e}_9) + \mathbf{e}_{10}^T \left(\frac{\hat{\mathbf{I}}_\eta \hat{\boldsymbol{\tau}}_\eta}{\mathbf{I}_\eta} + \mathbf{N} - \ddot{\boldsymbol{\eta}}_d + \mathbf{k}_9 \dot{\mathbf{e}}_9\right) \\
&\quad - \frac{\tilde{\mathbf{N}}\dot{\hat{\mathbf{N}}}}{\gamma_N} - \frac{\tilde{\mathbf{I}}_\eta \dot{\hat{\mathbf{I}}}_\eta}{\gamma_{I_\eta} \mathbf{I}_\eta} \\
&= \mathbf{e}_9^T (\mathbf{e}_{10} - \mathbf{k}_9 \mathbf{e}_9) + \mathbf{e}_{10}^T \left(\hat{\mathbf{N}} + \bar{\boldsymbol{\tau}}_\eta - \ddot{\boldsymbol{\eta}}_d + \mathbf{k}_9 \dot{\mathbf{e}}_9\right) \\
&\quad + \tilde{\mathbf{N}}\left(\mathbf{e}_{10} - \frac{\dot{\hat{\mathbf{N}}}}{\gamma_N}\right) - \frac{\tilde{\mathbf{I}}_\eta}{\gamma_{I_\eta} \mathbf{I}_\eta} (\dot{\hat{\mathbf{I}}}_\eta + \gamma_{I_\eta} \mathbf{e}_{10} \bar{\boldsymbol{\tau}}_\eta).
\end{aligned} \tag{37}$$

With the adaptive laws (23) and (25), we get that

$$\dot{V}_{\tau_\eta} = -\mathbf{k}_9 e_9^T e_9 - \mathbf{k}_{10} \mathbf{e}_{10}^T \mathbf{e}_{10} \le 0. \tag{38}$$

Consequently, from (29), (34), and (38), we obtain that

$$\dot{V} = \dot{V}_F + \dot{V}_\tau + V_{\tau_\eta} \le 0. \tag{39}$$

The errors defined in (16)-(18) converge to the origin asymptotically. □

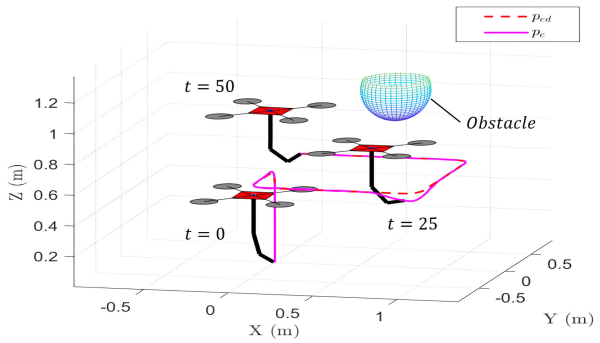

FIGURE 3. Scenario in the numerical examples.

In practice, Assumption 1 holds when the motion of the aerial manipulator is non-aggressive. However, it might not be fulfilled due to the mission's requirements. For example, if the aerial manipulator is expected to pick up an object and then release it to the desired position, the physical parameters could be considerably changed. In this case, the proposed theorem cannot be applied directly. As a future work, Assumption 1 is expected to be released to accommodate more conditions of missions.

IV. NUMERICAL SIMULATIONS

In this section, we present two numerical examples to illustrate the effectiveness of the proposed control scheme. The scenarios depicted in Figure 3 involve assigning a desired trajectory to the aerial manipulator system, which consists of two parts: taking off from the ground and executing a C-shaped trajectory. These examples are utilized to analyze and validate the performance of the control scheme in achieving accurate trajectory tracking and maneuvering of the aerial manipulator system. To demonstrate the effect of subtasks, the first example compares the results of no subtasks and the JAL subtask, and the second part is given with the OA subtask for the UAV. The comparisons in the two examples show the difference while applying the subtasks to the system. Note that the obstacle in the scenario is only considered in the second simulation , and no noise is applied to all signals.

A. EXAMPLE 1: SUBTASK - JAL

In the first simulation, the aerial manipulator system tracks a predetermined trajectory for the end effector, specifically focusing on the JAL subtask. The simulation results for $k_{sub} = 0$ and 1000 are included, which means with and without the subtask, to emphasize the effect of the JAL subtask. The gains in the proposed controllers are chosen as $\mathbf{k}_1 = \mathbf{k}_2 = \mathbf{k}_9 = \mathbf{k}_{10} = diag\{1,1,1\}$, $k_3 = k_4 = k_5 = k_6 = 10, k_7 = 6, k_8 = 2, \gamma_m = 1$, $\gamma_{F_q} = diag\{0.001, 0.001, 0\}, \gamma_{I_x} = \gamma_{I_y} = \gamma_{I_z} = 10^4, \gamma_\phi = \gamma_\theta = \gamma_\psi = \gamma_{x_q} = \gamma_{y_q} = 0.1, \gamma_N = \gamma_M = 1, \lambda = diag\{1,1,1\}$. The initial values of the variables are given as $\hat{m}(0) = 3.1, \hat{\mathbf{I}}(0) = [0.05, 0.05, 0.05]^T, \hat{\Theta}_\phi(0) = \hat{\Theta}_\theta(0) = \hat{\Theta}_\psi(0) = 1, \hat{\tau}_x(0) = \hat{\tau}_y(0) = 0$. The end-effector trajectories for both cases are illustrated in Fig. 4. As expected, the end-effector's position

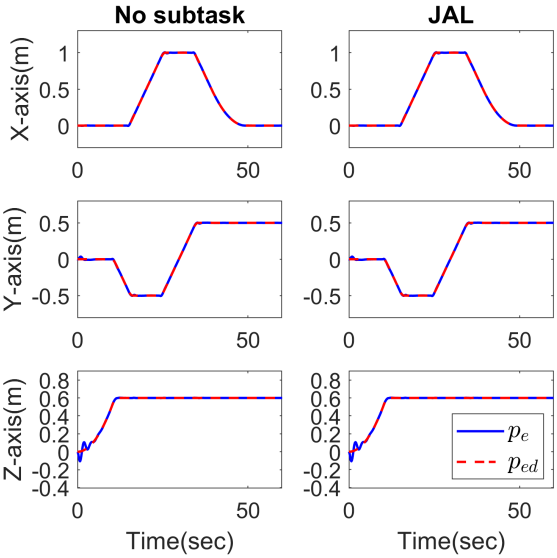

FIGURE 4. Trajectories of the end-effector with and without considering the JAL subtask.

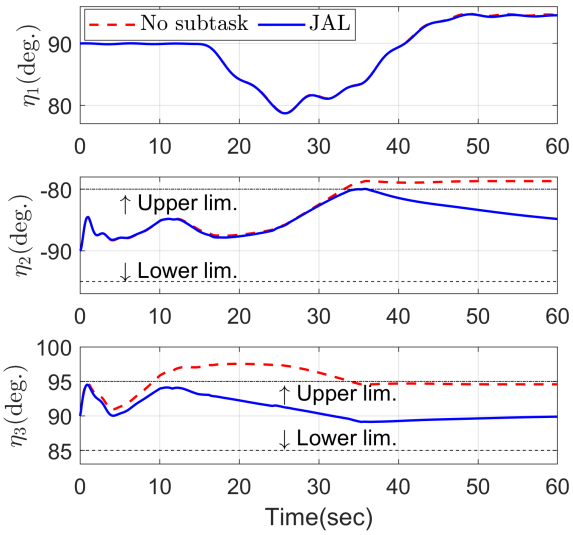

FIGURE 5. Joint angles of the robotic arm with and without the JAL subtask.

in both cases successfully follows the given trajectory. Although there are no significant differences in trajectories, the robotic arm's joint angles show obvious influence from the JAL subtask. Fig. 5 shows the joint angle of the robotic arm. After taking off, the joint angle remains in a predefined range for η_2 and η_3 while the JAL subtask is active. Therefore, we can learn that the proposed method can simultaneously reach the desired trajectory and subtask. Another numerical example with the OA subtask is then considered to verify this fact.

B. EXAMPLE 2: SUBTASK - OA

In this example, the subtask for avoiding obstacles for the UAV is considered. As in the illustration in Fig. 3, an obstacle placed in $\mathbf{p}_{ob} = [0.5, 0, 1.5]^T$ is set close to the desired trajectory of the end-effector. It is supposed to block the

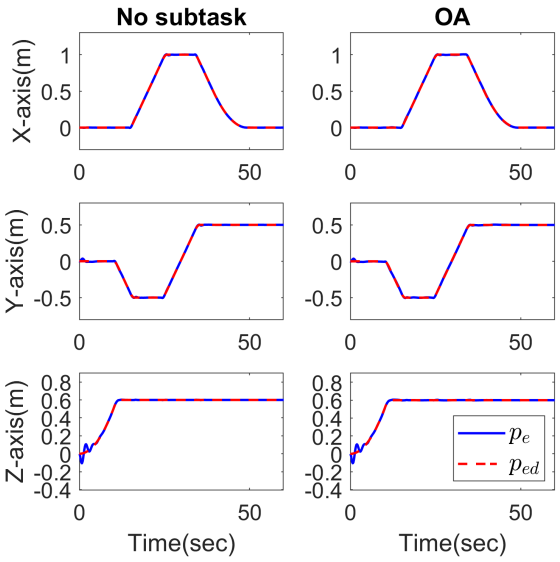

FIGURE 6. Trajectories of the end-effector with the OA subtask.

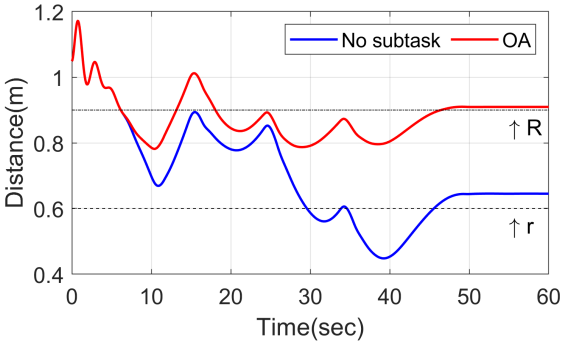

FIGURE 7. Distance between the UAV and the obstacle under the OA subtask.

UAV of the aerial manipulator system during the tracking task. Fig. 6 shows the tracking results of the end-effector with $k_{sub} = 0$ and 1, respectively. The difference between both cases is trivial and implies that the end-effector tracking is not affected by the OA subtask. Taking into account the results in Figs. 7 shows that the UAV successfully avoids the obstacle with the OA subtask. During the execution of the first scenario, if the UAV detects an obstacle within a distance less than the predefined threshold $R = 0.9$, as demonstrated in Figure 7 at $t = 8$ s, the obstacle avoidance mechanism is triggered. As a result, the UAV initiates a gradual movement away from the obstacle, ensuring that the distance between the UAV and the obstacle remains greater than the designated safety distance $r = 0.6$ at all times. Compared to the case without subtasks, we realize that the proposed method with the OA subtask works as expected. Finally, Fig. 8 is illustrated in detail for the difference in the end-effector's tracking error under each case. Although the purpose of the subtasks is different, there is no obvious difference in the magnitude of the tracking errors between different cases. Furthermore, the results indicate that the system can follow the assigned trajectory even if Assumption 1 is violated.

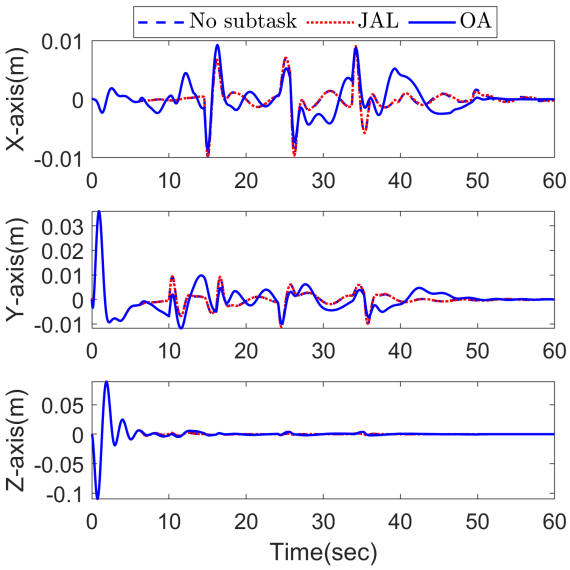

FIGURE 8. Comparison of the end-effector tracking error with the given subtasks.

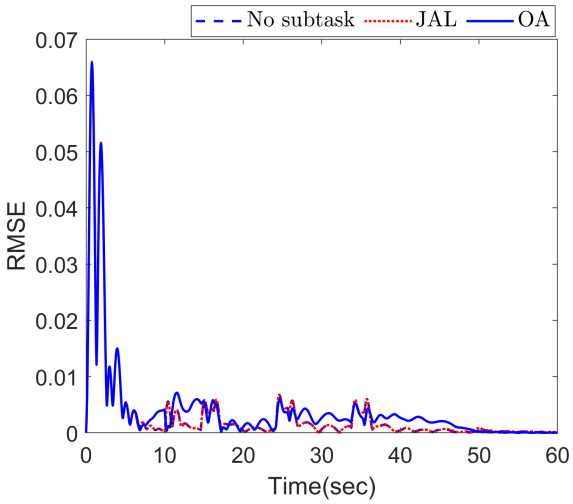

FIGURE 9. Comparison of the end-effector tracking RMSE with the given subtasks.

V. EXPERIMENT

In this section, the experimental results are presented to verify the proposed scheme in practice. The hardware setup is first introduced. The experimental data under the OA subtask are included to verify the results learned from the numerical examples.

A. HARDWARE SETUP

First of all, it is important to find the balance between payload and power consumption. We build an aerial manipulator composed of a hexarotor and a three-DOF robotic arm, as shown in Fig. 10 to afford the payload. For the hexarotor, its frame is chosen as ZD850 to have enough space to mount the robotic arm and place other components, including a Pixhawk 4 flight controller. Due to technical limitations, the attitude of the hexarotor is controlled by the built-in

FIGURE 10. The aerial manipulator in experiments.

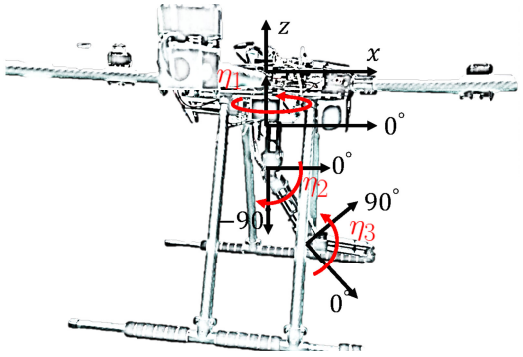

FIGURE 11. Coordinates of the robotic arm in experiments.

Pixhawk controller instead of the proposed torque controller. The desired attitude command is provided to Pixhawk at 200 Hz. To reduce power consumption, the parts of the robotic arm are produced by a 3D printer, and the length of each link is 0.13 m. Three servomotors, XM430-W-350-T designed by Dynamixel, are utilized as actuators for the robotic arm. The proposed robotic arm controller is implemented on Raspberry Pi 3 and OpenCR control boards to drive the servomotors. Due to the hardware limitation, this controller is running at 100 Hz. The weight of the hexarotor and the robotic arm is approximately 2.7 kg and 0.5 kg, respectively. The position of the hexarotor is detected by a motion capture (MOCAP) system developed by Optitrack at 120 Hz. The MOCAP data are then collected on a center station that runs the Robot Operating System (ROS). The adaptive backstepping controllers (10), (19), and (21) are implemented in the center station to calculate the desired commands for the hexarotor and the robotic arm. Meanwhile, the robotic arm encoders provide the joint angle to the center station to obtain its attitude for the proposed controllers. The control gains are given as $\mathbf{k}_1 = \mathbf{k}_2 = diag\{1, 1, 1\}, k_3 = diag\{2.2, 2.8, 4.1\}, \gamma_m = 0.1, \gamma_{F_q} = diag\{0.01, 0.01, 0\}, \lambda = diag\{0.05, 0.05, 0.1\}$. The initial values of the variables are given as $\hat{m}(0) = 3.1, \hat{\mathbf{I}}(0) = [0.05, 0.05, 0.05]^T, \hat{\Theta}_\phi(0) = \hat{\Theta}_\theta(0) = \hat{\Theta}_\psi(0) = 1, \hat{\tau}_x(0) = \hat{\tau}_y(0) = 0$.

B. EXPERIMENTAL RESULTS

To emphasize the effect of the proposed scheme, the results for the UAV with and without the collision avoidance subtask are presented as a comparison. The subtask OA was chosen

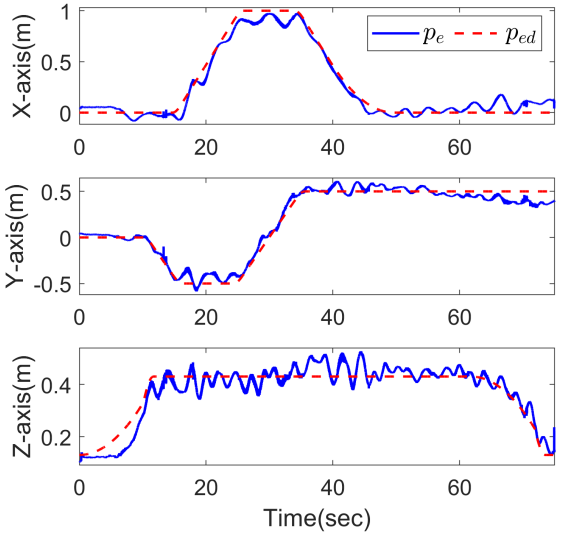

FIGURE 12. Profile of the end-effector's trajectory without subtasks.

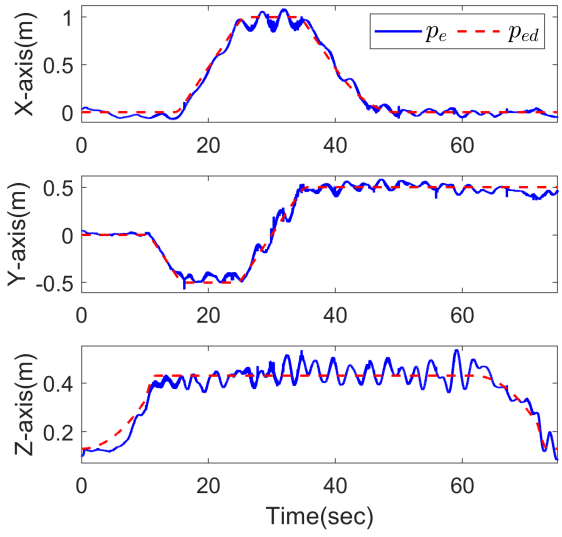

FIGURE 13. Profile of the end-effector's trajectory with the subtask of collision avoidance.

because it clearly shows the system moving away from the obstacle. The experiment scenario is similar to the simulation shown in Fig. 3. The obstacle is set on the ground rather than suspended upon the desired trajectory for ease of testing the system. We first present the result of tracking the desired end-effector trajectory with $k_{sub} = 0$, meaning there is no subtask in Fig. 12. The proposed tracking controller successfully follows the desired trajectory of the end-effector within an acceptable deviation. Then, we activate the OA subtask with $k_{sub} = 0.1$ and track the same trajectory. Fig. 13 shows the result with the subtask. The proposed tracking controller can follow the desired trajectory in both cases. The comparison of the tracking error of the end-effector shown in Fig. 14 further emphasizes this fact. Furthermore, the positions of the UAV with and without are illustrated in Fig. 15. To avoid an obstacle at $\mathbf{p}_{ob} = [0.974, 0.02, 0.165]^T$

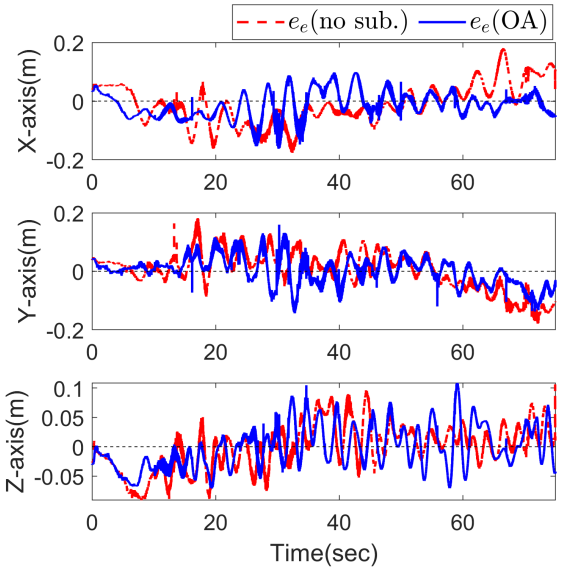

FIGURE 14. Comparison of the end-effectors' tracking errors with and without the subtask.

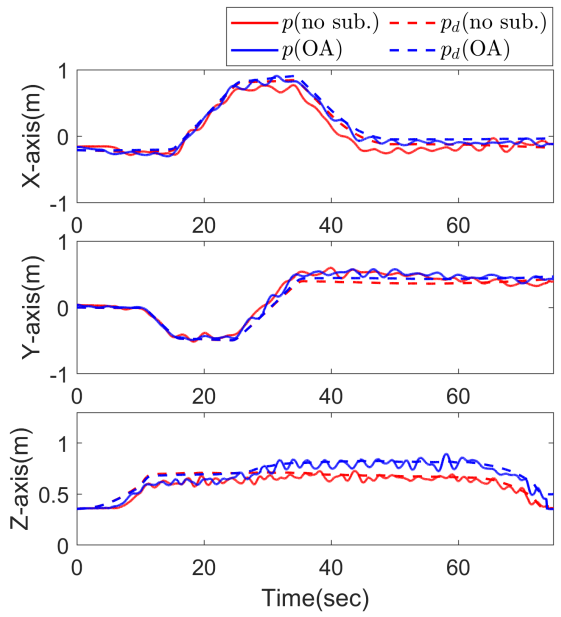

FIGURE 15. Comparison of the UAVs' trajectories with and without the subtask.

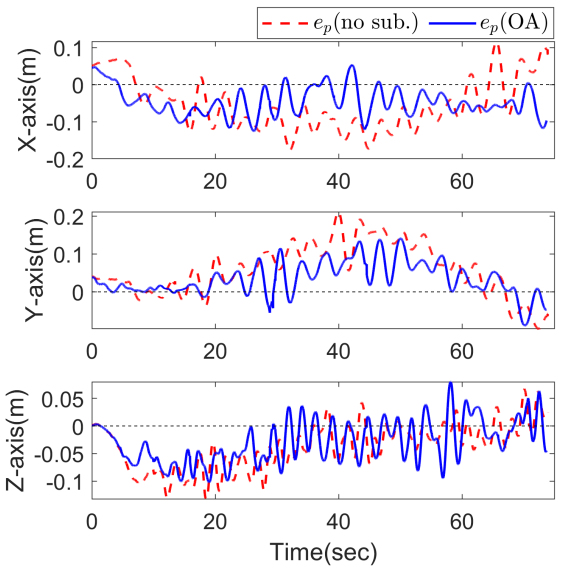

FIGURE 16. Comparison of the UAVs' tracking errors with and without the subtask.

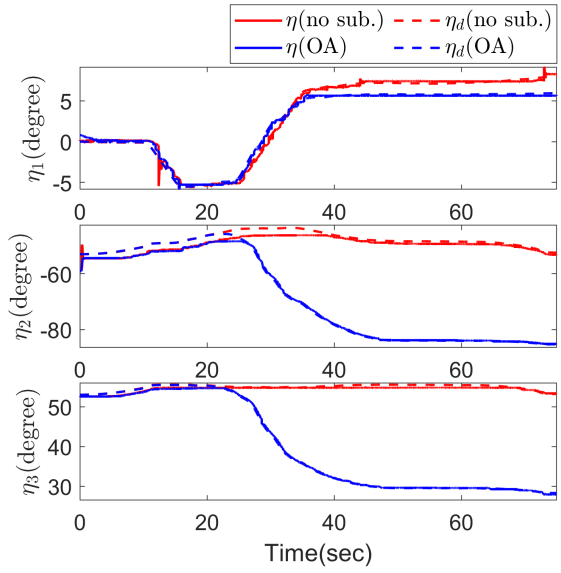

FIGURE 17. Comparison of the manipulators' joint angle with and without the subtask.

on the ground, the position of the UAV on the Z axis starts to increase with the given subtask of $t = 25$ s while the trajectory without subtasks is performed in lower altitude. The tracking errors of the UAV are shown in Fig. 16. It is evident that the subtask has no significant impact on the tracking errors. The end-effector's tracking errors for both cases are compared in Fig. 14. Even if the subtask for collision avoidance is assigned to the system, the tracking performance is still close to that without subtasks. This result matches the objective of the proposed multi-tasking method without degrading the main task's efficiency. On the other hand, the joint angles of the robotic arm show a tremendous difference between both cases, as shown in Fig.17. When the subtask is activated, the proposed controller significantly decreases η_2 and η_3. The robotic arm is dropped to keep the end-effector position as expected because the UAV increases altitude to avoid the obstacle. The comparison between the tracking errors of the robotic arm's joint angles under both cases is presented in Fig. 18 in detail. Note that the tracking error's magnitude in the Z-axis with no subtask increases at $t = 35$ s. This is due to the ground effect of the obstacle, which means that the UAV is very close to the obstacle. Thus, it is meaningful to implement the subtask of collision avoidance to improve the system's tracking performance.

In summary, the implemented control scheme enables the aerial manipulator to accurately follow the desired trajectory

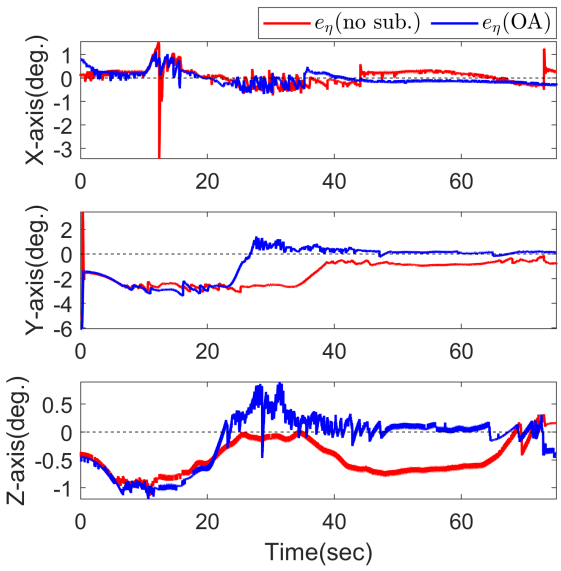

FIGURE 18. Comparison of the manipulators' joint angle tracking errors with and without the subtask.

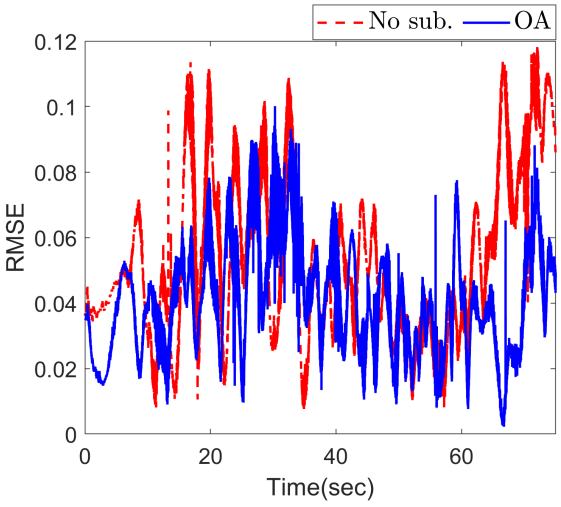

FIGURE 19. End-effector RMSE with and without subtasks.

of the end-effector while ensuring the UAV maintains a safe distance from obstacles. By choosing the subtask OA, it is obvious to demonstrate the effectiveness in the trajectory of the UAV under the given subtask. Meanwhile, the end-effector's trajectory tracking can still be kept without any significant increase in error because of the NSB strategy. The results show that the proposed system can transport the object smoothly. The high DOF is utilized to provide flexibility in the trajectories of both the UAV and the end-effector.

VI. CONCLUSION

A novel multi-tasking control scheme for aerial manipulators is proposed, combining NSB and adaptive backstepping control. The decoupled dynamic model is investigated under uncertainties to precisely control the motion of the UAV and the robotic arm. The system's redundancy is exploited for the design of subtasks using the NSB control strategy. According to the decoupled dynamics, the adaptive backstepping controllers for the aerial manipulator are developed to track the desired trajectories. The result is theoretically proved under Assumption 1 regarding slow-changing uncertainties and disturbance, which might lead to the limitation on performance. However, the numerical examples still show the efficacy of our method, including various subtasks. For further validation in practice, the experiment with the subtask of collision avoidance is included. All results indicate that the proposed design can track the given trajectories and achieve the subtask simultaneously with an RMSE error of approximately 5 cm. In future work, the collaboration between multiple aerial manipulators will be considered.

ACKNOWLEDGMENT

The authors would like to thank the anonymous reviewers and the editor for their valuable comments that significantly improved this work.

REFERENCES

[1] S. Say, H. Inata, J. Liu, and S. Shimamoto, "Priority-based data gathering framework in UAV-assisted wireless sensor networks," *IEEE Sensors J.*, vol. 16, no. 14, pp. 5785–5794, Jul. 2016.

[2] K. Dorling, J. Heinrichs, G. G. Messier, and S. Magierowski, "Vehicle routing problems for drone delivery," *IEEE Trans. Syst., Man, Cybern., Syst.*, vol. 47, no. 1, pp. 70–85, Jan. 2017.

[3] C. J. Salaan, K. Tadakuma, Y. Okada, Y. Sakai, K. Ohno, and S. Tadokoro, "Development and experimental validation of aerial vehicle with passive rotating shell on each rotor," *IEEE Robot. Autom. Lett.*, vol. 4, no. 3, pp. 2568–2575, Jul. 2019.

[4] N. Masmoudi, W. Jaafar, S. Cherif, J. B. Abderrazak, and H. Yanikomeroglu, "UAV-based crowd surveillance in post COVID-19 era," *IEEE Access*, vol. 9, pp. 162276–162290, 2021.

[5] K. Gkountas and A. Tzes, "Leader/follower force control of aerial manipulators," *IEEE Access*, vol. 9, pp. 17584–17595, 2021.

[6] S. R. Nekoo, D. Feliu-Talegon, J. A. Acosta, and A. Ollero, "A 79.7g manipulator prototype for E-flap robot: A plucking-leaf application," *IEEE Access*, vol. 10, pp. 65300–65308, 2022.

[7] D. Matouk, O. Gherouat, F. Abdessemed, and A. Hassam, "Quadrotor position and attitude control via backstepping approach," in *Proc. 8th Int. Conf. Modeling, Identificat. Control (ICMIC)*, Nov. 2016, pp. 73–79.

[8] M. Huang, B. Xian, C. Diao, K. Yang, and Y. Feng, "Adaptive tracking control of underactuated quadrotor unmanned aerial vehicles via backstepping," in *Proc. Amer. Control Conf.*, Jun./Jul. 2010, pp. 2076–2081.

[9] B. Zhao and D. Yue, "Disturbance observer based nonlinear robust attitude tracking controller for a hexarotor UAV," in *Proc. 37th Chin. Control Conf. (CCC)*, Jul. 2018, pp. 9996–10001.

[10] B. Xiao and S. Yin, "A new disturbance attenuation control scheme for quadrotor unmanned aerial vehicles," *IEEE Trans. Ind. Informat.*, vol. 13, no. 6, pp. 2922–2932, Dec. 2017.

[11] D. Brescianini and R. D'Andrea, "Computationally efficient trajectory generation for fully actuated multirotor vehicles," *IEEE Trans. Robot.*, vol. 34, no. 3, pp. 555–571, Jun. 2018.

[12] Y. Wang, J. Sun, H. He, and C. Sun, "Deterministic policy gradient with integral compensator for robust quadrotor control," *IEEE Trans. Syst., Man, Cybern., Syst.*, vol. 50, no. 10, pp. 3713–3725, Oct. 2020.

[13] H. Sun, W. Zhang, R. Yu, and Y. Zhang, "Motion planning for mobile robots—Focusing on deep reinforcement learning: A systematic review," *IEEE Access*, vol. 9, pp. 69061–69081, 2021.

[14] B. Ma, Z. Liu, W. Zhao, J. Yuan, H. Long, X. Wang, and Z. Yuan, "Target tracking control of UAV through deep reinforcement learning," *IEEE Trans. Intell. Transp. Syst.*, vol. 24, no. 6, pp. 5983–6000, Jun. 2023.

[15] A. Ollero, M. Tognon, A. Suarez, D. Lee, and A. Franchi, "Past, present, and future of aerial robotic manipulators," *IEEE Trans. Robot.*, vol. 38, no. 1, pp. 626–645, Feb. 2022.

[16] V. Ghadiok, J. Goldin, and W. Ren, "Autonomous indoor aerial gripping using a quadrotor," in *Proc. IEEE/RSJ Int. Conf. Intell. Robots Syst.*, Sep. 2011, pp. 4645–4651.
[17] D. Mellinger, Q. Lindsey, M. Shomin, and V. Kumar, "Design, modeling, estimation and control for aerial grasping and manipulation," in *Proc. IEEE/RSJ Int. Conf. Intell. Robots Syst.*, Sep. 2011, pp. 2668–2673.
[18] X. Liang, Y. Fang, N. Sun, and H. Lin, "Nonlinear hierarchical control for unmanned quadrotor transportation systems," *IEEE Trans. Ind. Electron.*, vol. 65, no. 4, pp. 3395–3405, Apr. 2018.
[19] D. Sanalitro, H. J. Savino, M. Tognon, J. Cortés, and A. Franchi, "Full-pose manipulation control of a cable-suspended load with multiple UAVs under uncertainties," *IEEE Robot. Autom. Lett.*, vol. 5, no. 2, pp. 2185–2191, Apr. 2020.
[20] R. Miyazaki, H. Paul, T. Kominami, and K. Shimonomura, "Wire-suspended device control based on wireless communication with multirotor for long reach-aerial manipulation," *IEEE Access*, vol. 8, pp. 172096–172104, 2020.
[21] M. Tognon, E. Cataldi, H. A. T. Chavez, G. Antonelli, J. Cortés, and A. Franchi, "Control-aware motion planning for task-constrained aerial manipulation," *IEEE Robot. Autom. Lett.*, vol. 3, no. 3, pp. 2478–2484, Jul. 2018.
[22] F. Caccavale, G. Giglio, G. Muscio, and F. Pierri, "Adaptive control for UAVs equipped with a robotic arm," *IFAC Proc. Volumes*, vol. 47, no. 3, pp. 11049–11054, 2014.
[23] G. Heredia, A. E. Jimenez-Cano, I. Sanchez, D. Llorente, V. Vega, J. Braga, J. A. Acosta, and A. Ollero, "Control of a multirotor outdoor aerial manipulator," in *Proc. IEEE/RSJ Int. Conf. Intell. Robots Syst.*, Sep. 2014, pp. 3417–3422.
[24] Y. Chen, W. Zhan, B. He, L. Lin, Z. Miao, X. Yuan, and Y. Wang, "Robust control for unmanned aerial manipulator under disturbances," *IEEE Access*, vol. 8, pp. 129869–129877, 2020.
[25] G. Nava, Q. Sablé, M. Tognon, D. Pucci, and A. Franchi, "Direct force feedback control and online multi-task optimization for aerial manipulators," *IEEE Robot. Autom. Lett.*, vol. 5, no. 2, pp. 331–338, Apr. 2020.
[26] J. Liang, Y. Chen, Y. Wu, Z. Miao, H. Zhang, and Y. Wang, "Adaptive prescribed performance control of unmanned aerial manipulator with disturbances," *IEEE Trans. Autom. Sci. Eng.*, vol. 20, no. 3, pp. 1804–1814, Jul. 2023.
[27] Y. Chen, J. Liang, Y. Wu, Z. Miao, H. Zhang, and Y. Wang, "Adaptive sliding-mode disturbance observer-based finite-time control for unmanned aerial manipulator with prescribed performance," *IEEE Trans. Cybern.*, vol. 53, no. 5, pp. 3263–3276, May 2023.
[28] P. O. Pereira, R. Zanella, and D. V. Dimarogonas, "Decoupled design of controllers for aerial manipulation with quadrotors," in *Proc. IEEE/RSJ Int. Conf. Intell. Robots Syst. (IROS)*, Oct. 2016, pp. 4849–4855.
[29] S. Thapa, H. Bai, and J. Á. Acosta, "Cooperative aerial manipulation with decentralized adaptive force-consensus control," *J. Intell. Robotic Syst.*, vol. 97, no. 1, pp. 171–183, Jan. 2020.
[30] D. Lee, J. Byun, and H. J. Kim, "RISE-based trajectory tracking control of an aerial manipulator under uncertainty," *IEEE Control Syst. Lett.*, vol. 6, pp. 3379–3384, 2022.
[31] Y.-C. Liu and C.-Y. Huang, "DDPG-based adaptive robust tracking control for aerial manipulators with decoupling approach," *IEEE Trans. Cybern.*, vol. 52, no. 8, pp. 8258–8271, Aug. 2022.
[32] Y.-C. Liu, "Task-space coordination control of bilateral human–swarm systems," *J. Franklin Inst.*, vol. 352, no. 1, pp. 311–331, 2015.
[33] G. Antonelli, F. Arrichiello, and S. Chiaverini, "The null-space-based behavioral control for autonomous robotic systems," *Intell. Service Robot.*, vol. 1, no. 1, pp. 27–39, 2008.
[34] K. Baizid, G. Giglio, F. Pierri, M. A. Trujillo, G. Antonelli, F. Caccavale, A. Viguria, S. Chiaverini, and A. Ollero, "Experiments on behavioral coordinated control of an unmanned aerial vehicle manipulator system," in *Proc. IEEE Int. Conf. Robot. Autom. (ICRA)*, May 2015, pp. 4680–4685.
[35] G. Muscio, F. Pierri, M. A. Trujillo, E. Cataldi, G. Giglio, G. Antonelli, F. Caccavale, A. Viguria, S. Chiaverini, and A. Ollero, "Experiments on coordinated motion of aerial robotic manipulators," in *Proc. IEEE Int. Conf. Robot. Autom. (ICRA)*, May 2016, pp. 1224–1229.
[36] G. Muscio, F. Pierri, M. A. Trujillo, E. Cataldi, G. Antonelli, F. Caccavale, A. Viguria, S. Chiaverini, and A. Ollero, "Coordinated control of aerial robotic manipulators: Theory and experiments," *IEEE Trans. Control Syst. Technol.*, vol. 26, no. 4, pp. 1406–1413, Jul. 2018.
[37] S. Kim, S. Choi, and H. J. Kim, "Aerial manipulation using a quadrotor with a two DOF robotic arm," in *Proc. IEEE/RSJ Int. Conf. Intell. Robots Syst.*, Nov. 2013, pp. 4990–4995.
[38] Y.-C. Liu and T.-W. Ou, "Non-linear adaptive tracking control for quadrotor aerial robots under uncertain dynamics," *IET Control Theory Appl.*, vol. 15, no. 8, pp. 1126–1139, 2021.
[39] Y.-C. Liu and N. Chopra, "Control of semi-autonomous teleoperation system with time delays," *Automatica*, vol. 49, no. 6, pp. 1553–1565, Jun. 2013.

KAI-YUAN LIU (Member, IEEE) received the B.S. degree in power mechanical engineering from National Tsing Hua University, Hsinchu, Taiwan, in 2015. He is currently pursuing the Ph.D. degree with the Department of Mechanical Engineering, National Cheng Kung University, Tainan, Taiwan.

His research interests include bilateral teleoperation, aerial robotics, and multi-agent systems.

TE-KANG HUNG received the B.S. degree in mechanical engineering from National Chung Cheng University, Chiayi, Taiwan, in 2021. He is currently pursuing the M.S. degree with the Department of Mechanical Engineering, National Cheng Kung University, Tainan, Taiwan.

His research interests include null-space control and aerial manipulator systems.

CHI-HUNG LIN received the B.S. degree in mechanical engineering from National Chiao Tung University, Hsinchu, Taiwan, in 2019, and the M.S. degree in mechanical engineering from National Cheng Kung University, Tainan, Taiwan, in 2022.

His research interests include null-space control and aerial manipulator systems.

YEN-CHEN LIU (Senior Member, IEEE) received the B.S. and M.S. degrees in mechanical engineering from National Chiao Tung University, Hsinchu, Taiwan, in 2003 and 2005, respectively, and the Ph.D. degree in mechanical engineering from the University of Maryland, College Park, MD, USA, in 2012.

He is currently a Professor with the Department of Mechanical Engineering, National Cheng Kung University (NCKU), Tainan, Taiwan. His research interests include control of networked robotic systems, bilateral teleoperation, multi-robot systems, mobile robot networks, and human–robot interaction. He was a recipient of the Ta-You Wu Memorial Award from the Ministry of Science and Technology (MOST), Taiwan, in 2016; the Kwoh-Ting Li Researcher Award from National Cheng Kung University, in 2018; the Young Scholar Fellowship-Columbus Program from MOST, in 2019; and the Best Young Professional Member Award from the IEEE Tainan Section, in 2020.